INTERNATIONAL JOURNAL FOR NUMERICAL AND ANALYTICAL METHODS IN GEOMECHANICS
Int. J. Numer. Anal. Meth. Geomech. (2016)
Published online in Wiley Online Library (wileyonlinelibrary.com). DOI: 10.1002/nag.2549

Discrete element modeling of dynamic behaviors of railway ballast under cyclic loading with dilated polyhedra

S. Ji[1,*,†], S. Sun[1] and Y. Yan[2]

[1]*State Key Laboratory of Structural Analysis for Industrial Equipment, Dalian University of Technology, Dalian 116023, China*
[2]*School of Civil and Safety Engineering, Dalian Jiaotong University, Dalian 116028, China*

SUMMARY

The dynamic behaviors of railway ballast under cyclic loading are simulated with discrete element method (DEM). Dilated polyhedra are constructed based on the Minkowski sum operator in order to resemble the irregular shapes of ballast particles. The polyhedral particle generation, contact detection between particles and contact laws are presented. Ballast box tests with periodic lateral boundaries are conducted to simulate the dynamics of the sleeper and ballast particles. The settlement and effective stiffness of ballast bed are investigated under cyclic loadings with five distinct frequencies. The settlement of ballast bed is significant in the first several cycles and increases with the number of cycles gradually. The higher frequency loading generates larger displacement in the same simulation time. The effective stiffness of ballast bed increases gradually. To study the effect of particles' sharpness, dilated polyhedra with different dilating radii and spherical particles are also developed. Simulation results show the sharper the ballast particles are, the smaller the produced settlement. Copyright © 2016 John Wiley & Sons, Ltd.

Received 7 November 2014; Revised 19 April 2016; Accepted 25 May 2016

KEY WORDS: railway ballast; discrete element method; Minkowski sum; cyclic loading; settlement; dilated polyhedra

1. INTRODUCTION

Under the long term action of train loadings, the elastic stiffness of railway ballast track is reduced, accompanying the increase of accumulated settlement of ballast bed. Investigations on dynamic behaviors of ballast bed under cyclic loadings are helpful in improving the ballast bed performance and design. Previous studies on the deformation and degradation of ballast bed include field measurements [1, 2] and laboratory model tests [3–5] and numerical simulations [6, 7].

For numerical simulations of dynamic behaviors of ballast bed, continuum approaches have been applied to determine the stress distribution and deformation [2, 8, 9]. However, the ballast bed is inherently a large collection of discrete particles. Properties of the constitutive ballast particles, such as the shape and gradation, unavoidably influence the dynamic behaviors of ballast bed as a whole. Unfortunately, continuum methods cannot take into account these microscopic properties. Recently, the discrete element method (DEM), as a powerful tool for granular materials modeling, has been applied widely to simulate the dynamic behaviors of ballast [10–14]. In the DEM simulations of ballast, clumps of overlapping spheres or bonding spheres were generated to resemble the irregular shapes of ballast particles [13, 15–18]. The overlapping method has the advantage of describing the real sizes and irregular shapes of ballasts exactly [7, 16, 19]. The bonding method is more suitable

*Correspondence to: Shunying Ji, State Key Laboratory of Structural Analysis for Industrial Equipment, Dalian University of Technology, Dalian 116023, China.
†E-mail: jisy@dlut.edu.cn

for the simulation of irregularly shaped ballast particle's breakage, because it is capable of describing arbitrary shapes and allowing breakage under external loadings at the same time [6, 7, 11, 15, 20]. In both methods, one ballast particle may be constructed with hundreds or thousands of spheres [21]. The computational efficiency is tremendously lowered because of the huge number of spheres used in the DEM simulations. This limits its engineering applications. Therefore, polygonal and polyhedral models were developed to model the irregular ballast particles [12, 22, 23].

Recently, dilated polyhedral models, more efficient and accurate for programming and computation, have been developed to model the irregular rock rubbles. The generation of a dilated polyhedron element is based on the theory of Minkowski sum with the combination of Voronoi diagram [24–29]. A basic polyhedron is generated using Voronoi diagram with defined sizes and shapes randomly. The polyhedron is dilated by placing the center of a sphere at every point of the polyhedron surface based on the classical concept of Minkowiski sum. In this way, the vertices and edges of the original polyhedron become spheres and cylinders with hemi-spherical ends. The sharpness of a dilated polyhedron can be adjusted by changing the dilating sphere radius. The inter-element contact detection and contact force calculation can be performed succinctly and are easy to implement.

For the investigations of railway ballast dynamic behaviors, triaxial tests were carried out to identify the maximum stress level, the strength and stiffness changes during the cyclic loading process [5, 30, 31]. The triaxial tests were also used to determine the breakage ratio of ballast particles under different loading levels [32, 33]. The loading frequency plays a significant role in the settlement and elastic behaviors of ballast materials. The higher the loading frequency is, the more settlement the ballast bed performances [34]. On the other hand, ballast box tests were also conducted to study the dynamic behaviors of ballast under the train loading and tamping. Compared with triaxial tests, ballast box tests correlate with ballast field performance, providing data on the settlement, stiffness and amount of degradation [14].The DEM simulations were also performed and compared with the physical experiments [15]. Both physical tests and DEM simulations show box tests are suitable to investigate the dynamic behaviors of ballast under cyclic loading. Moreover, mechanical properties of ballast bed are greatly influenced by the particles shapes and loading frequencies of cyclic loadings [6, 7, 32, 35].

Therefore, dilated polyhedral particles are generated to resemble the irregularly shaped ballast in this study. The contact detection and contact force law of dilated polyhedra are presented in detail. The dynamic behaviors of ballast are simulated under cyclic loadings with various frequencies. The settlement and effective stiffness of ballast bed are studied and analyzed. Moreover, the influence of ballast particles' sharpness is studied.

2. DISCRETE ELEMENT MODEL WITH DILATED POLYHEDRA

To describe the irregular shapes of ballast particles, dilated polyhedral elements are constructed. The inter-locking effect of irregular ballast can be modeled. For the contact detection of ballast particles, various contact patterns are developed considering the vertices, edges and faces of polyhedra. The inter-element contact force model is also introduced here.

2.1. Construction of dilated polyhedral particles

To construct a dilated polyhedral element, a basic polyhedron is defined first with vertices, edges and faces. The polyhedral faces are generated with a series of triangle planes. A sphere with radius r is then adopted to sweep all the vertices, edges and faces of the polyhedron without changing their relative orientations [26]. The center of the dilating sphere is located on the surface of the basic polyhedron. Consequently, the original vertices turn into spheres. The edges turn into cylinders with hemi-spherical ends. The faces turn into plates with a certain thickness. With this approach, a dilated polyhedral element is generated with rounded edges and corners.

Figure 1(a) shows a dilated polyhedron, including 30 vertices, 84 edges and 56 faces. The average polyhedral radius is 25 mm, which is calculated as the arithmetic mean of all the distances from the

DOI: 10.1002/nag

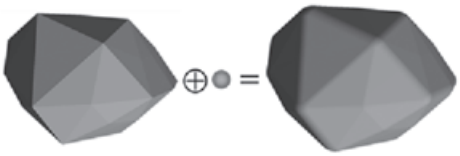

(a) Schematic of a dilated polyhedron generation

(b) Dilating radius r =0.5mm (c) Dilating radius r =20mm

Figure 1. Generation of a dilated polyhedron.

vertices to the mass center of the particle. The sharpness of the dilated polyhedron is dominated by the dilating sphere radius. Figure 1(b) and (c) show clearly the two dilated polyhedral elements constructed with the same basic polyhedron but with different sphere radii of 0.5 mm and 20 mm, respectively. The larger the sphere radius is, the smoother the dilated polyhedron is. The dilated polyhedron returns to its basic polyhedron as the sphere radius approaches zero.

Figure 2 shows various dilated polyhedra generated. The above particle generation method results in contact simplicity. However, the computational efficiency depends on the numbers of vertices and faces of particles. The more the numbers of vertices and faces, the more contact detections and calculations will be. Also, an appropriate contact detection algorithm is introduced to reduce the computational efficiency to $O(N)$, where N is the number of vertices [26, 28, 29].

2.2. Neighbor search and contact detection of dilated polyhedral elements

Two sets of Eulerian coordinates, global and local, are chosen to describe the position and orientation of a polyhedron. The origins of the two coordinates are located at the computational domain and the mass center of the dilated polyhedron, respectively. The global coordinate system is used to describe the particle's translation motion and mass center, while the local one is used to describe the rotational motion of the particle. The quaternion approach is adopted to transfer the motion and force information between the two coordinates [17, 36].

1. Neighbor search

All dilated polyhedral elements are sorted and stored based on their mass center positions in a three dimensional Cartesian grids. The grid length is slightly larger than the maximum size of all particles. A list of all elements potentially in contact is determined first through its surrounding grids.

A distance parameter ε is introduced here. When the distance between two dilated polyhedral elements δ_{ij} is less than ε, this neighbor pair is added in the neighbor list. In this study, the

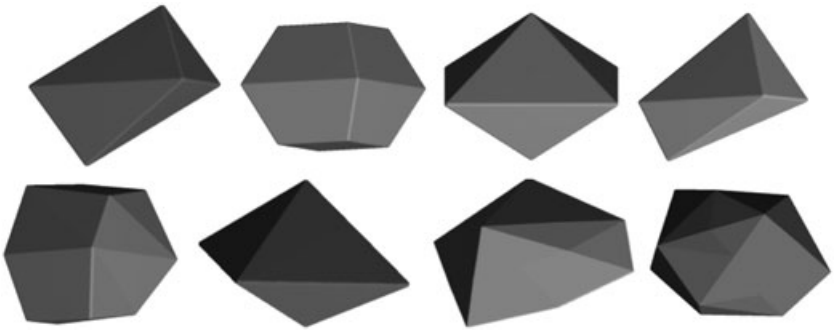

Figure 2. Generated dilated polyhedra.

DOI: 10.1002/nag

parameter ε is proportional to the relative normal velocity of the two elements and the intervals of the neighborhood.

The distance between any two dilated elements can be determined as,

$$\delta_{ij} = \Delta_{ij}\text{-}r_i - r_j \tag{1}$$

where$\delta_{ij}$is the distance between the two dilated polyhedra i and j, Δ_{ij} is the distance between the two corresponding basic polyhedra and r_i and r_j are the dilating sphere radii of the two dilated elements, respectively.

2. Contact detection

The dilated polyhedral model is composed of vertices, edges and faces. The possible contact modes can be classified into three categories: edge–edge contact, vertex–face contact and face–face contact.

For an edge–edge contact as shown in Figure 3(a), the contact detection is related to the determination of the shortest distance vector Δ between the two line segments P_1P_2 and $P_1^{'}P_2^{'}$ as shown in Figure 3(b), where P_1P_2 and $P_1^{'}P_2^{'}$ are the axes of the two edges, and P_{C1} and P_{C2} are intersections of the distance vector Δ and the two edges. Thus, the distance δ between the two elements is calculated as $\delta = |\Delta| - r_i - r_j$. If $\delta < 0$, the two particles are in contact.

If point P_{C1} or point P_{C2} is at the end of line segments, the edge–edge contact becomes vertex–edge contact as shown in Figure 3(c). The projection of the sphere center O_1 on the edge is first obtained and defined as point P as shown in Figure 3(d). The corresponding distance is calculated as $\delta = |\mathbf{PO}_1|\text{-}r_i - r_j$. If both of the intersections are at the end of line segments, the edge–edge contact becomes vertex–vertex contact.

For a vertex–face contact as shown in Figure 4(a), the projection of the sphere center O_1 on the face is first defined as point P as shown in Figure 4(b). If point P is in the plane, the two dilated polyhedra may be in contact. The corresponding distance is calculated as $\delta = |\mathbf{PO}_1|\text{-}r_i - r_j$. If $\delta < 0$, the two particles are in contact.

A face–face contact is shown in Figure 5. This kind of contact actually has infinite number of contact points. To simplify the calculations, it can be simplified as multiple-point contacts on the contacting faces. Only those points belonging to edge–edge and vertex–face contacts are considered in the DEM simulations. All of these contact points generate a polygon, and the area of the polygon

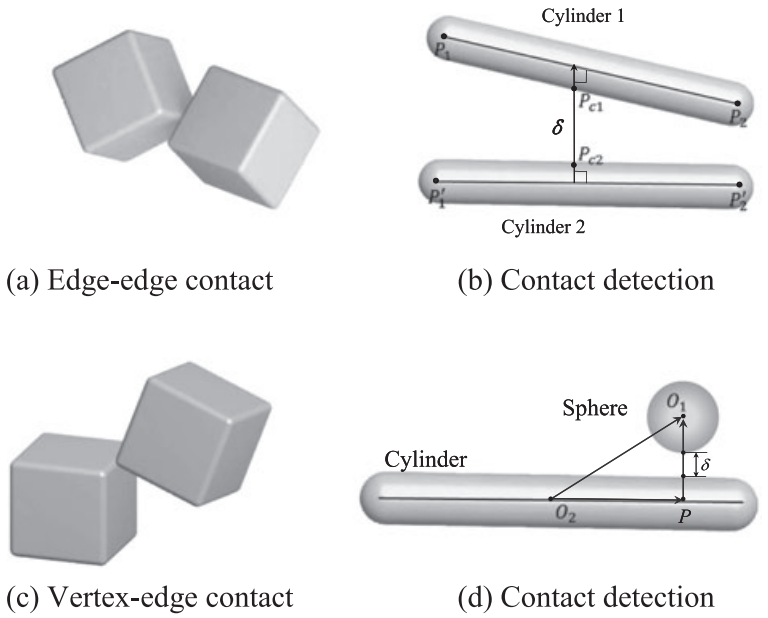

Figure 3. Edge-edge contact of two dilated polyhedra.

DOI: 10.1002/nag

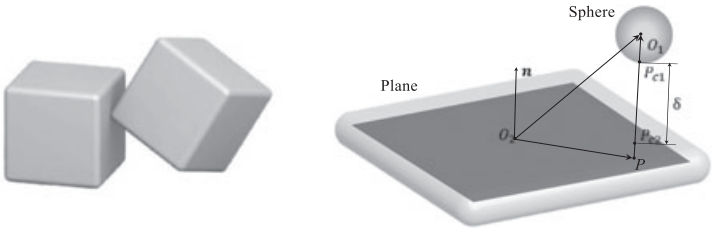

(a) Vertex-face contact (b) Contact detection

Figure 4. Vertex-face contact of two dilated polyhedra.

can be calculated. In this case, the contact area is a quadrilateral. An edge–face contact is included in the face–face contact.

2.3. *Contact force model*

For the interaction between any two particles in contact, elastic contact forces are considered in the normal and tangential directions. With the overlap determined during contact detection, the elastic normal contact force is calculated as,

$$\mathbf{F}_{\mathrm{n}} = k_n \delta \tag{2}$$

where F_{n} is the elastic normal contact force, k_n is the normal stiffness and δ is the overlap between the two contacting polyhedra determined in the previous section.

For edge–edge and vertex–face contacts, the nonlinear Hertzian contact model is adopted. This model has been applied widely in the contact simulations of granular materials [37, 38].The corresponding normal stiffness can be written as,

$$k_n = \frac{4G\sqrt{R_e \delta}}{3(1-\nu)} \tag{3}$$

where G and ν are the shear modulus and Poisson ratio of granular materials, and R_{e} is the equivalent radius of the curvature of the contacting particles. In edge–edge contacts, the curvatures are different for the contacts happening in different relative orientations. The curvature equal to the radius of the dilating sphere is used to simplify the programming.

For face–face contacts, the change of the contact area induces different overlap. However, this change is relatively small. Ignoring the influence of the contact area under different deformations, the linear model is used and the normal stiffness can be written as [39],

$$k_n = \frac{AE}{2R_e N} \tag{4}$$

where A is the face–face contact area. N is the number of points in contact.

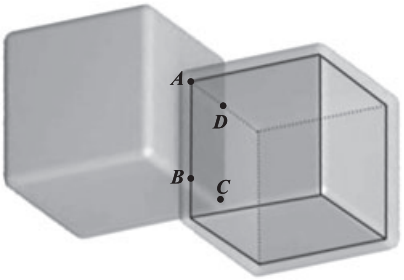

Figure 5. Face-face contact of two dilated polyhedra.

DOI: 10.1002/nag

The elastic tangential contact force is determined with the overlap in the tangential direction, which can be obtained incrementally in each time step. At time step m, the tangential force vector is calculated from the tangential force at the previous time step $(m-1)$, and can be calculated as,

$$\mathbf{F}_{\mathrm{t}}^{m} = \mathbf{F}_{\mathrm{t}}^{m-1} - [k_{\mathrm{t}} \cdot \Delta t(\mathbf{V}_{AB} - \mathbf{V}_{AB} \cdot \mathbf{n})] \tag{5}$$

where $\mathbf{F}_{\mathrm{t}}^{m}$ and $\mathbf{F}_{\mathrm{t}}^{m-1}$ are the tangential forces at time steps m and $m-1$, respectively. k_{t} is the tangential contact stiffness, $\mathbf{V}_{AB}$ is the relative velocity of the two dilated polyhedra A and B and $\mathbf{n}$ is the unit vector in the normal direction; Δt is the time step.

The tangential stiffness is dependent on the normal force, and can be expressed as [38],

$$k_{\mathrm{t}} = \beta k_n and\ \beta = 3(1-v)/(2-v). \tag{6}$$

The relative velocity of the two dilated polyhedra in contact can be calculated as,

$$\mathbf{V}_{AB} = \mathbf{V}_A - \mathbf{V}_B + (\mathbf{r}_A \times \boldsymbol{\omega}_A) - (\mathbf{r}_B \times \boldsymbol{\omega}_B) \tag{7}$$

where $\mathbf{r}_A$ and $\mathbf{r}_B$ are the position vectors from the sphere center to the contact points, and $\boldsymbol{\omega}_A$and $\boldsymbol{\omega}_B$are the angular velocities of particles A and B, respectively.

Based on the Mohr–Coulomb friction law, the tangential contact force is limited with the sliding friction, and can be written as,

$$\mathbf{F}_{\mathrm{t}}^{m} = \min\left(\left|\mathbf{F}_{\mathrm{t}}^{m}\right|, \mu\left|\mathbf{F}_{\mathrm{n}}^{m}\right|\right) \cdot \mathbf{t} \tag{8}$$

where μ is the friction coefficient, and $\mathbf{t}$ is the unit vector in the tangential direction in the current contact.

Damping force is also considered here. It is proportional to the relative velocity,

$$F_d = 2\varsigma\sqrt{mk_n}\mathbf{V}_{AB} \cdot \mathbf{n} \tag{9}$$

where m is the mean mass of the two colliding particles, and ς is related to particle's coefficient of restitution ε. Based on the theoretical solution for binary contacts, an explicit relationship between ς and ε can be written as,

$$\varsigma = \frac{-\ln\varepsilon}{\sqrt{\pi^2 + \ln^2\varepsilon}}. \tag{10}$$

With the inter-element contact forces, the moments on the dilated polyhedra can also be determined by the vector from the mass center of polyhedra to the contact point. With the contact force and moments obtained at each time step, the velocity and displacement of each dilated polyhedron are updated step by step. The equations that define translational and rotational motion are standard central difference equations. The matrix that defines the orientation of each element is calculated with quaternion approach.

3. DEM SIMULATIONS OF BALLAST UNDER CYCLIC LOADING

The dynamic behaviors of ballast are investigated though ballast box tests. The settlement and effective stiffness of ballast bed are studied considering the influence of loading frequencies and particles' sharpness.

DOI: 10.1002/nag

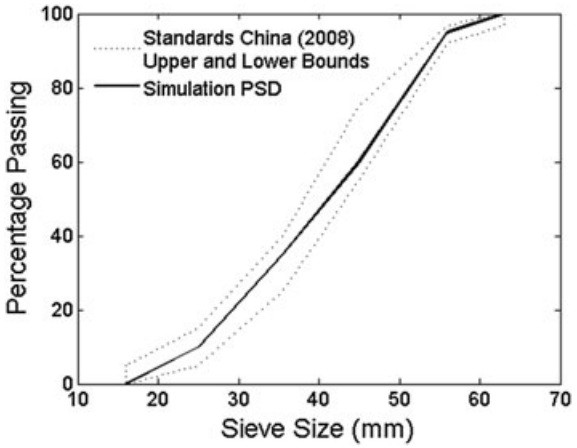

Figure 6. Gradation of ballast used in the DEM simulations.

3.1. *Setup of the ballast box test in DEM simulation*

The settlement of ballast is found to be sensitive to its aggregate gradation [1]. Figure 6 shows the particle size distribution (PSD) curve of ballast based on China standards 2008, which is representative of ballast used in the field in China. Particles of each size range are first weighed separately and mixed thoroughly. All particles are then dropped into a box of length 700 mm and width 300 mm under the action of gravity. Next, after ballast particles come to static state,

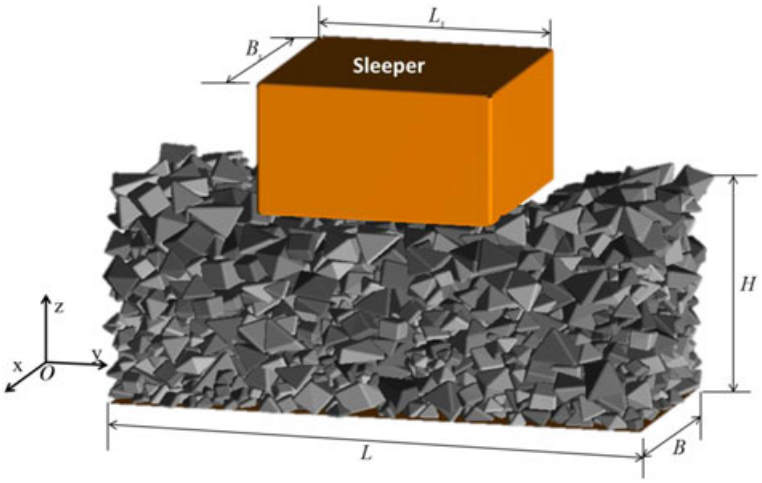

Figure 7. The DEM model of the ballast box test.

Table I. Main parameters used in the simulation.

Parameters	Symbols	Values
Ballast density	ρ	2600 kg/m^3
Shear modulus	G	20 GPa
Poisson's ratio	ν	0.3
Coefficient of restitution	ε	0.8
Coefficient of sliding friction	μ	0.5
Time step	dt	2.1×10^{-6} s
Total mass of ballast	M	110 kg

DOI: 10.1002/nag

a wall is applied and loaded with a sinusoidal loading at a frequency of 3 Hz on the top for a couple of seconds to make the ballast particles achieve the initial compacted state. The amplitude of the sinusoidal loading is from 0 kN to 10 kN. Finally, the top wall is removed and

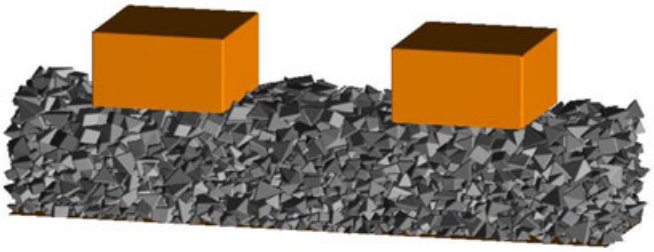

(a) Domain width L=1400mm

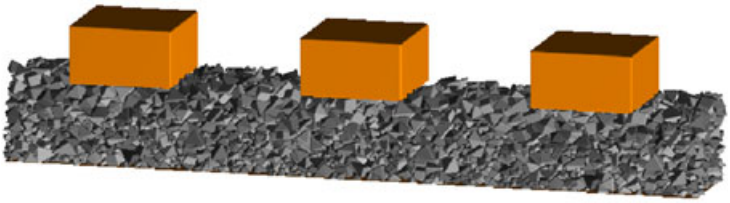

(b) Domain width L=2100mm

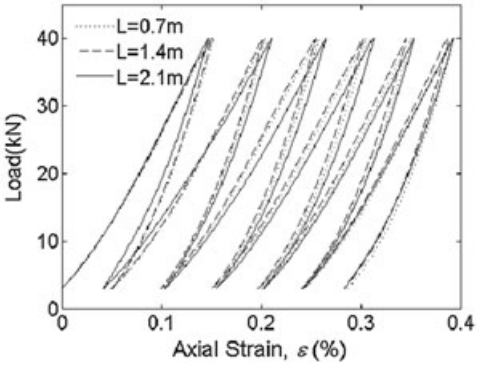

(c) Variation of cyclic load with axial strain at various domain widths

Figure 8. Influence of domain width.

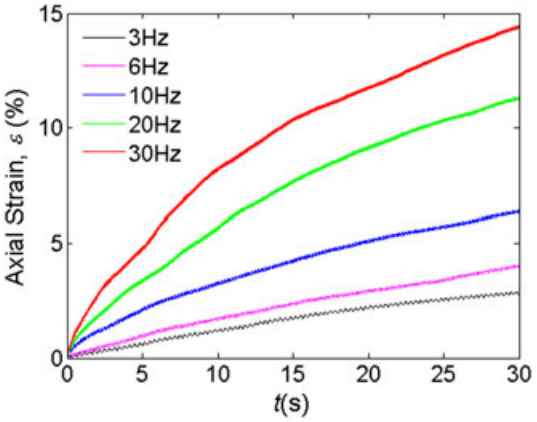

Figure 9. The axial strain under various cyclic loading frequencies.

DOI: 10.1002/nag

a sleeper of length 300 mm, width 300 mm and mass 34 kg is placed on the top of ballast until ballast comes to static state.

After the initial preparation, a cyclic loading is applied on the sleeper. To model the dynamic behaviors of ballast bed on large scale, periodic boundaries are applied in the y direction of the computational domain. When a particle passes through one side of the boundary, this particle will re-enter on the opposite side with the same velocity and orientation. Also, only the vertical displacement of the sleeper is considered under the action of external cyclic loading and the resistance of ballast particles. Figure 7 shows the DEM model of the box test, in which ballast particles are constructed with the dilating sphere of radius 4 mm. Main computational parameters are listed in Table I.

The domain width of 700 mm is based on the work of McDowell [14]. In order to check the influence of domain width, two additional widths of 1400 mm and 2100 mm are used, resulting in two and three sleepers resting on ballast as shown in Figure 8(a) and (b). Figure 8(c) plots the variation of cyclic load with axial strain at various domain widths under 6-Hz loading frequency. Axial strain is defined as the ratio of the

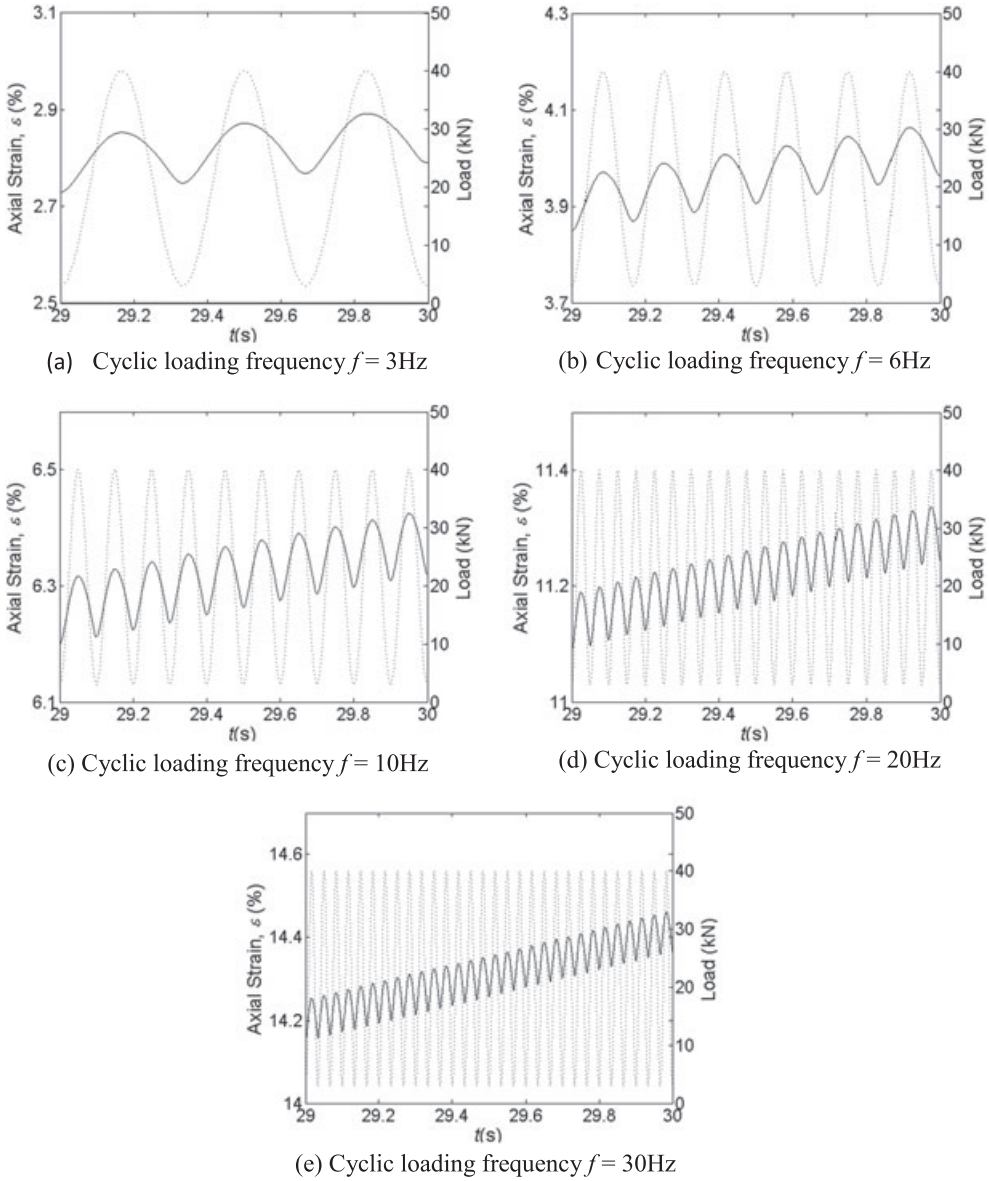

(a) Cyclic loading frequency f = 3Hz

(b) Cyclic loading frequency f = 6Hz

(c) Cyclic loading frequency f = 10Hz

(d) Cyclic loading frequency f = 20Hz

(e) Cyclic loading frequency f = 30Hz

Figure 10. The enlarged sleeper displacement under various loading frequencies.

DOI: 10.1002/nag

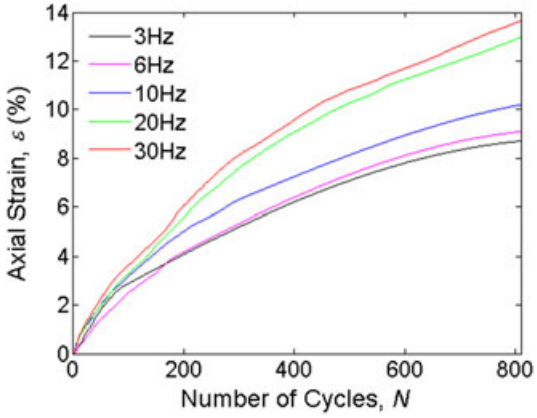

Figure 11. Variation of axial strain with number of cycles at different frequencies.

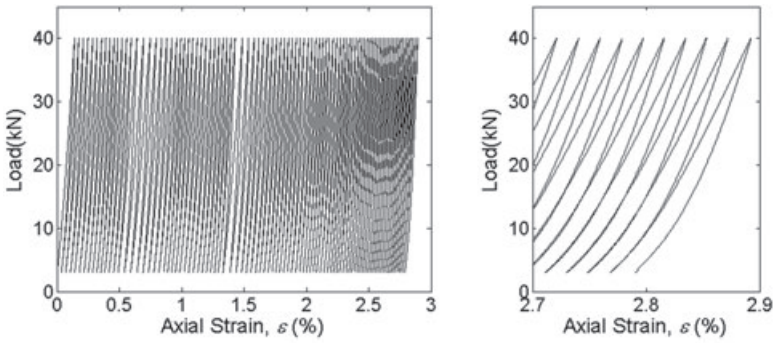

(a) Cyclic loading frequency f = 3Hz

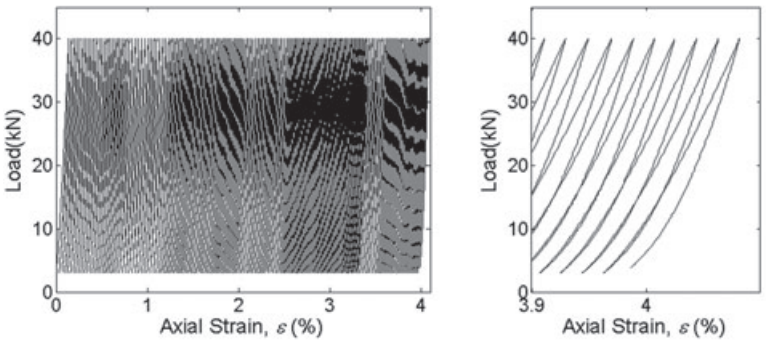

(b) Cyclic loading frequency f = 6Hz

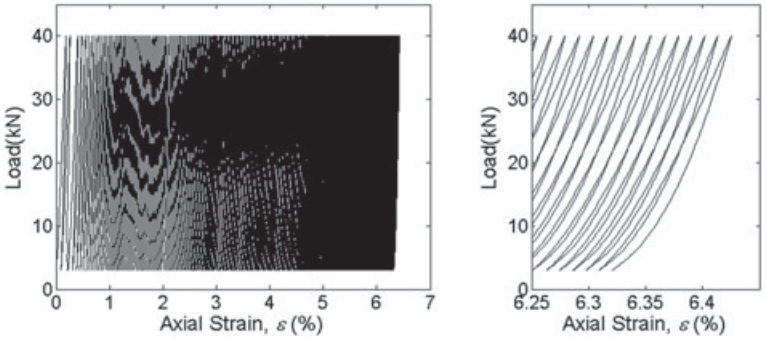

(c) Cyclic loading frequency f = 10Hz

Figure 12. Cyclic load versus axial strain under various loading frequencies.

DOI: 10.1002/nag

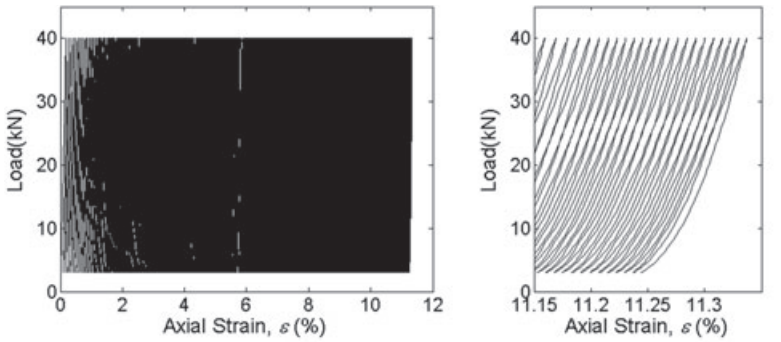

(d) Cyclic loading frequency f = 20Hz

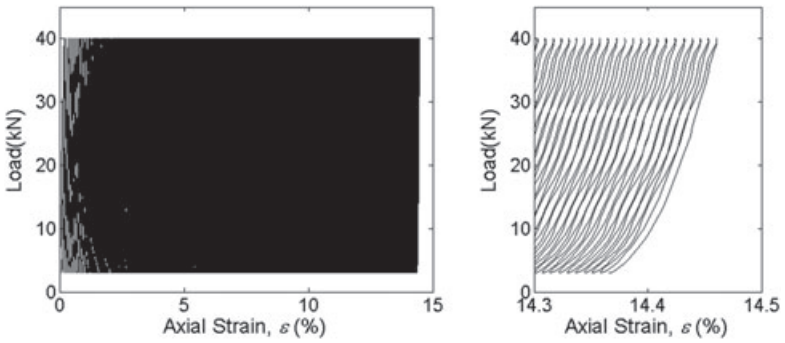

(e) Cyclic loading frequency f = 30Hz

Figure 12. Continued.

sleeper settlement to the initial thickness of ballast bed. The curves are very close and the influence of the domain width can be ignored. The domain width of 700 mm is used in the following studies.

3.2. *Simulation results under various cyclic loading frequencies*

The loading frequency of traffic loading is about 8–10 Hz for a normal train. For a high speed train, loading frequency may reach 30 Hz [30]. Because of the increasing demand of high speed trains, five loading frequencies of 3 Hz, 6 Hz, 10 Hz, 20 Hz and 30 Hz are chosen here. The magnitude of these cyclic loadings is in the range of [3 kN, 40 kN] with a harmonic function. Figure 9 plots the axial strain of the sleeper. It shows that the axial strain increases continuously with fluctuation. During the same loading period, the higher the loading frequency is, the larger the axial strain is.

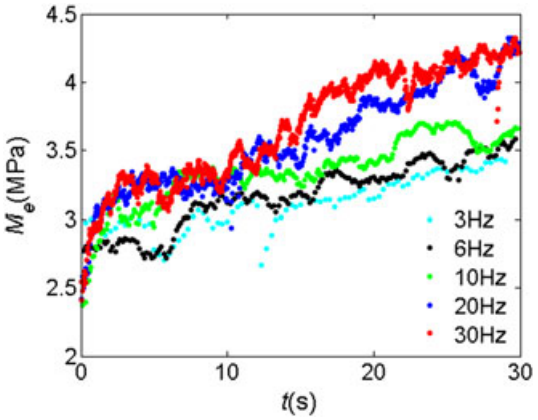

Figure 13. The effective stiffness versus simulation time.

DOI: 10.1002/nag

Figure 10 gives the enlarged views of axial strain and cyclic load during the last second under various cyclic loading frequencies. It is clear to see the strain fluctuates synchronously with the cyclic load. In one cycle of the cyclic loading, the minimum strain corresponds to the minimum load. The minimum strain in every cycle is defined as the permanent strain.

Figure 11 plots the variation of axial strain with number of cycles at various frequencies. The curves become smooth after 200 cycles of loading, and a significant increase presents in strain for high values of frequencies. The simulation results are in agreement with those presented in Indraratna *et al*. [6].

Figure 12 shows the load-axial strain curves, and the enlarged view of corresponding final 1-mm settlement. During one cycle, the ballast bed presents both the elastic and the plastic deformation. The elastic deformation is proportional to the loading magnitude, while the plastic deformation is induced by the rearrangement and reorientation of particles. The elastic deformation is recovered when the external force is removed. The plastic deformation is accumulated with the number of loading cycles, which is the so-called granular ratcheting [26].

For any loading frequency, the primary loading cycles produce significant plastic deformations because of the initial loose packing of ballast. The rate of permanent settlement increase reduces as the number of cycle increases. This is also consistent with the laboratory data of Indraratna and Nimbalkar [40].

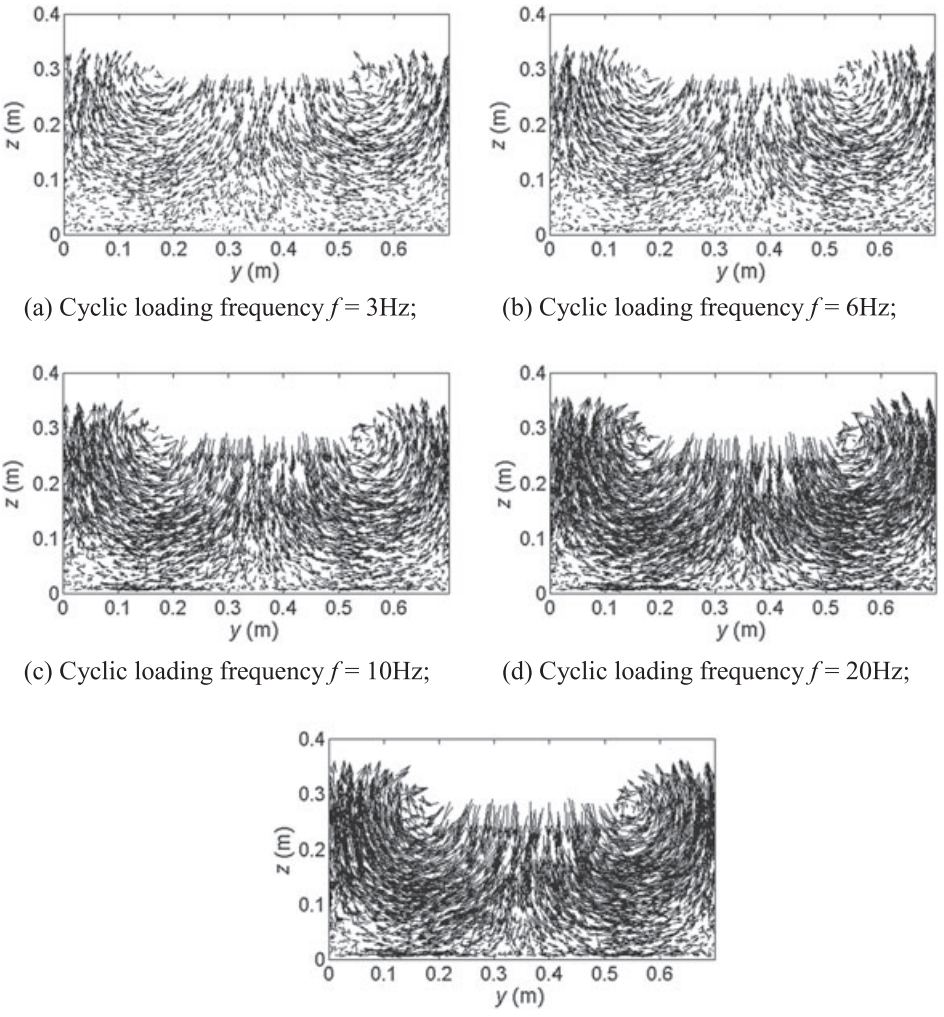

(a) Cyclic loading frequency f = 3Hz; (b) Cyclic loading frequency f = 6Hz;

(c) Cyclic loading frequency f = 10Hz; (d) Cyclic loading frequency f = 20Hz;

(e) Cyclic loading frequency f = 30Hz;

Figure 14. The displacement vectors of ballast particles at the end of simulation.

DOI: 10.1002/nag

The effective stiffness is an important parameter for ballast bed. Figure 13 shows the effective stiffness M_e as a function of simulation time. M_e generally increases with simulation time. The effective stiffness is different under different loading frequencies. The higher the frequency, the bigger the effective stiffness is.

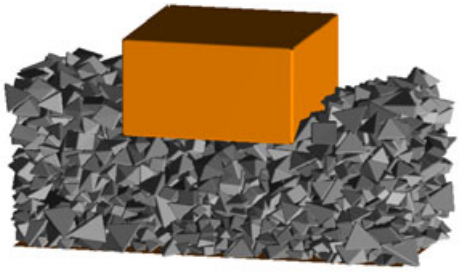

(a) Dilating radius r=3.5mm;

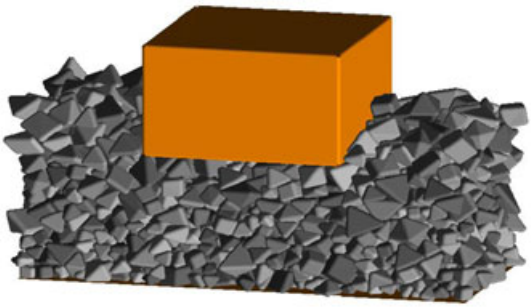

(b) Dilating radius r= 6mm;

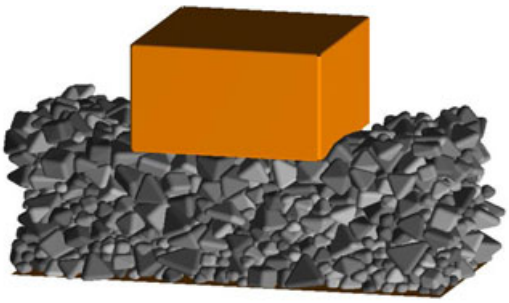

(c) Dilating radius r= 8mm;

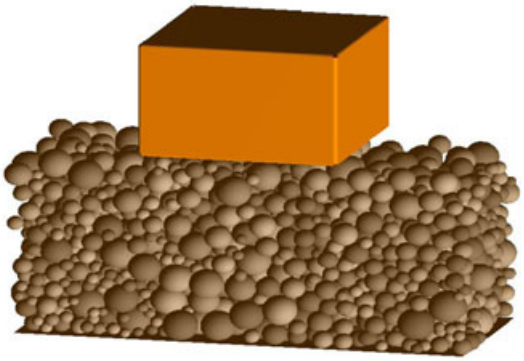

(d) Spherical particles as ballast particles

Figure 15. The DEM models of box tests with different dilating radii.

DOI: 10.1002/nag

Figure 14 plots the displacement vectors of ballast particles at the end of the simulations. It clearly shows the particles beneath the sleeper move downward. The amplitudes of displacements decrease as the distance from the sleeper increases. It approaches zero at the bottom of the ballast box. The ballast particles on both sides of the sleeper move upward, while the particles in the middle layer move laterally. These characteristics are consistent with the work of Lu and McDowell, in which ballast particles were generated with clumps of spheres [7]. As the number of loading cycles increases, two vortexes are generated. The main reason is the rearrangement process and the dense packing of ballast particles. This phenomenon is clearer for high values of frequencies for the same simulation duration.

Table II. Physical parameters of DEM models with different particle shapes.

Parameters	Number of particles	Initial ballast bed thickness	Bulk density	Time step
$r = 3.5$ mm	2453	0.268 m	1954.5 kg/m^3	1.9×10^{-6} s
$r = 4$ mm	2337	0.31 m	1689.7 kg/m^3	2.1×10^{-6} s
$r = 6$ mm	2112	0.30 m	1746 kg/m^3	2.23×10^{-6} s
$r = 8$ mm	1672	0.27 m	1940 kg/m^3	2.51×10^{-6} s
Spherical model	2312	0.34 m	1540.6 kg/m^3	1.3×10^{-6} s

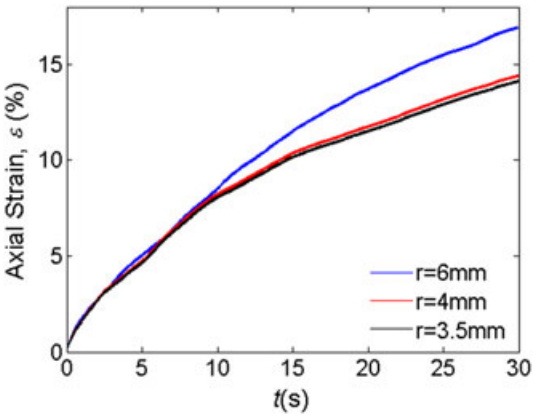

Figure 16. Axial strain versus simulation time of sharper models at loading frequency $f = 30$ Hz.

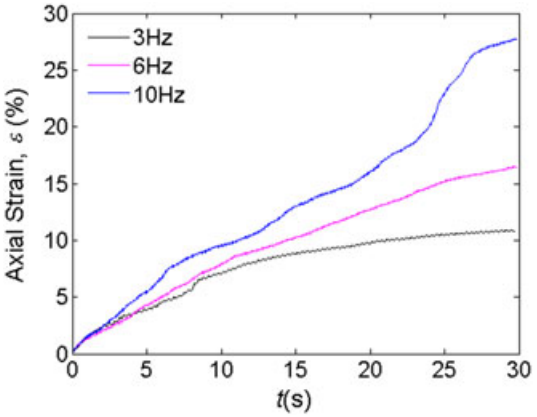

Figure 17. Axial strain of smooth model under various cyclic loading frequencies.

DOI: 10.1002/nag

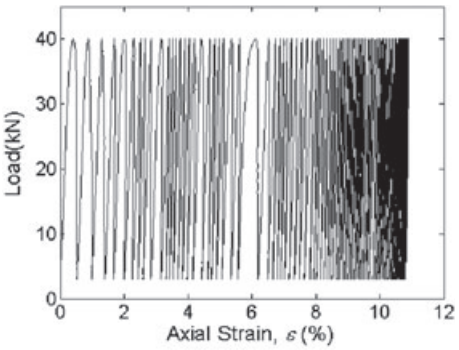

(a) Cyclic loading frequency f = 3Hz;

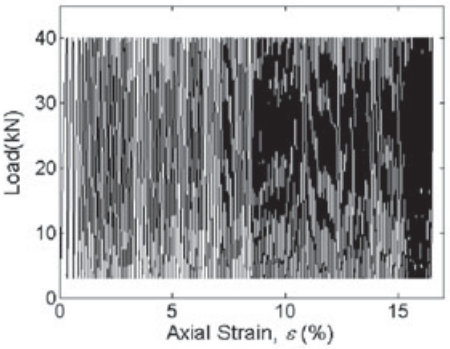

(b) Cyclic loading frequency f = 6Hz;

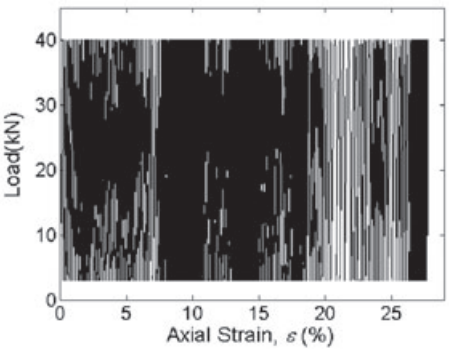

(c) Cyclic loading frequency f = 10Hz;

Figure 18. Cyclic load versus axial strain of smooth model under various loading frequencies.

3.3. Particles' sharpness effect

To investigate the influence of particles' sharpness on the dynamic behaviors of ballast, four additional particle shapes are constructed besides dilated polyhedra with the dilating sphere of radius 4 mm. They are dilated polyhedra with the dilating radius of 3.5 mm, 6 mm, 8 mm and spherical particles. Figure 15 shows the corresponding DEM models. Some of the physical parameters are calculated and listed in Table II with the same particle size distribution and the same total mass.

Figure 16 illustrates the axial strain with the simulation time for dilating radius $r = 3.5$ mm, 4 mm and 6 mm at loading frequency $f = 30$ Hz. Simulation results show particles with smaller dilating radii (sharp model) generate less axial strain.

Figure 17 shows the axial strain with simulation time for dilating radius $r = 8$ mm (smooth model) at various frequencies. The ballast bed settlements are larger compared with those of $r = 4$ mm shown in Figure 9. Especially for the 10-Hz case, the settlement increases rapidly during the simulation time from 23 s to 27 s. The main reason is the permanent settlement induced by the rearrangement of

DOI: 10.1002/nag

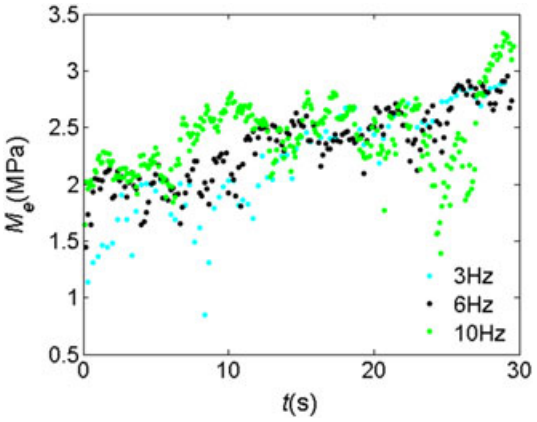

Figure 19. The effective stiffness versus simulation time of the smooth model.

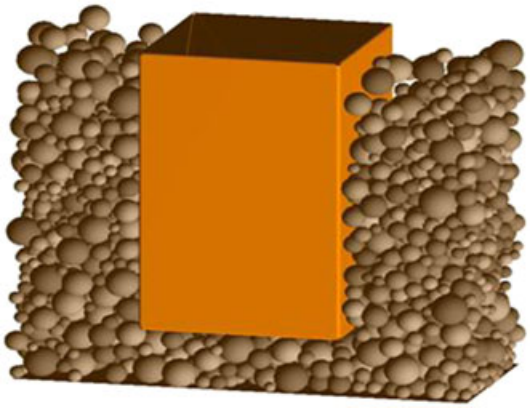

Figure 20. The sleeper falling into the ballast bed in the spherical model case.

ballast particles under cyclic loading. Ballasts particles are rearranged more easily for smoother model. The axial strain is up to 27% at the end of the simulation, which is too big. The resultant thickness of the ballast bed is less than 0.2 m, which cannot meet railroad track standards for ballast bed thickness requirements.

Figures 18 and 19 show the load-axial strain curves and the effective stiffness of the smooth model under various loading frequencies. The effective stiffness does not exhibit obvious change rules as those shown in Figure 13 of the sharper model. This may be because the thinner thickness of the ballast bed of the smooth model.

For the spherical model, the sleeper moves into the ballast bed within one period of loading and keeps going down as shown in Figure 20. The ballast box tests under cyclic loading cannot be numerically simulated with spheres here because spheres cannot provide necessary interlock between particles.

4. CONCLUSIONS

The dynamic behaviors of ballast are investigated through ballast box tests with periodic boundaries under cyclic loadings using DEM. To model the irregular shapes of ballast particles, dilated polyhedral elements are generated with a basic polyhedron and a dilating sphere based on Minkowski sum approach. The sharpness of the generated ballast particle is dominated by the radius

DOI: 10.1002/nag

of dilating sphere. The neighbor search algorithm, contact force model for this dilated polyhedron particle model are also presented in detail.

The dynamic behaviors of ballast bed are analyzed under five various loading frequencies in terms of axial strain and the effective stiffness of ballast bed. Vortex fields of the ballast particles in the ballast box are observed in the DEM simulations. The influence of loading frequencies on the ballast behaviors on macro scale is significant. Five kinds of ballast particles are constructed to study the particles' sharpness effect. The sharper particles generate significant inter-locking effect. Consequently, sharper particles can reduce the permanent settlement of the ballast bed, and are better to support the sleeper.

For future studies, more thorough parametric studies will be performed to analyze statistically the ballast dynamic behaviors considering the ballast shape, size and the loading features. The dilated polyhedral model with breakage will also be developed to study the ballast bed behaviors under the influence of crush failure of ballast particles.

ACKNOWLEDGEMENTS

The authors appreciate the discussions on the dilated polyhedron model with Professor Hayley H. Shen of Clarkson University, USA and Dr. Hopkins Mark A of US Army Cold Regions Research and Engineering Laboratory (CREEL). This study is financially supported by the National Natural Science Foundation of China (41176012, U12342092, 11572067) and the National Program on Key Basic Research Project of China (973 Program) (2010CB731502).

REFERENCES

1. Tutumluer E, Qian Y, Hashash YM, Ghaboussi J, Davis DD. Discrete element modelling of ballasted track deformation behaviour. *International Journal of Rail Transportation* 2013; **1**:57–73.
2. Zhai WM, Wang KY, Lin JH. Modeling and experiment of railway ballast vibrations. *Journal of Sound and Vibration* 2004; **270**(4–5):673–683.
3. Al-Saoudi NKS, Hassan KH. Behavior of track ballast under repeated loading. *Geotechnical and Geological Engineering* 2014; **32**:167–178.
4. Kennedy J, Woodward PK, Medero G, Banimahd M. Reducing railway track settlement using three-dimensional polyurethane polymer reinforcement of the ballast. *Construction and Building Materials* 2013; **44**:615–625.
5. Suiker ASJ, Selig ET, Frenkel R. Static and cyclic triaxial testing of ballast and subballast. *Journal of Geotechnical and Geoenvironmental Engineering* 2005; **131**(6):771–782.
6. Indraratna B, Thakur PK, Vinod JS. Experimental and numerical study of railway ballast behavior under cyclic loading. *International Journal of Geomechanics* 2010; **10**(4):136–144.
7. Lu M, McDowell GR. The importance of modelling ballast particle shape in the discrete element method. *Granular Matter* 2007; **9**(1–2):69–80.
8. Rajesh S, Choudhary K, Chandra S. A generalized model for geosynthetic reinforced railway tracks resting on soft clays. *International Journal for Numerical and Analytical Methods in Geomechanics* 2015; **39**:310–326.
9. Ricci L, Nguyen VH, Sab K, Duhamel D, Schmitt L. Dynamic behaviour of ballasted railway tracks: a discrete/continuous approach. *Computers and Structures* 2005; **83**:2282–2292.
10. Elias J. Simulation of railway ballast using crushable polyhedral particles. *Powder Technology* 2014; **264**:458–465.
11. Hossain Z, Indraratna B, Darve F, Thakur PK. DEM analysis of angular ballast breakage under cyclic loading. *Geomechanics and Geoengineering* 2007; **2**(3):175–181.
12. Huang H, Tutumluer E. Discrete Element Modeling for fouled railroad ballast. *Construction and Building Materials* 2011; **25**:3306–3312.
13. Lobo-Guerrero S, Vallejo L. Discrete element method analysis of rail track ballast degradation during cyclic loading. *Granular Matter* 2006; **8**(3–4):195–204.
14. McDowell GR, Lim WL, Collop AC, Armitage R, Thom NH. Comparison of ballast index tests for railway trackbeds. *Geotechnical Engineering* 2004; **157**:151–161.
15. Lim WL, McDowell GR. Discrete element modelling of railway ballast. *Granular Matter* 2005; **7**(1):19–29.
16. Ngo NT, Indraratna B, Rujikiatkamjorn C. DEM simulation of the behaviour of geogrid stabilised ballast fouled with coal. *Computers and Geotechnics* 2014; **55**:224–231.
17. Yan Y, Ji S. Discrete element modeling of direct shear tests for a granular material. *International Journal for Numerical and Analytical Methods in Geomechanics* 2010; **34**(9):978–990.
18. Zeng YW, Jin L, Du X, Gao R. Refined modeling and movement characteristics analyses of irregularly shaped particles. *International Journal for Numerical and Analytical Methods in Geomechanics* 2015; **39**:388–408.
19. Gao R, Du X, Zeng Y, Li Y, Yan J. A new method to simulate irregular particles by discrete element method. *Journal of Rock Mechanics and Geotechnical Engineering* 2012; **4**(3):276–281.
20. Ergenzinger C, Seifried R, Eberhard P. A discrete element model predicting the strength of ballast stones. *Computers and Structures* 2012; **108/109**:3–13.

DOI: 10.1002/nag

21. Ferellec JF, McDowell GR. Modelling realistic shape and particle inertia in DEM. *Geotechnique* 2010; **60**(3):227–232.
22. Huang H, Chrismer S. Discrete element modeling of ballast settlement under trains moving at "Critical Speeds". *Construction and Building Materials* 2013; **38**:994–1000.
23. Saussine G, Cholet C, Gautier PE, Dubois F, Bohatier C, Moreau JJ. Modelling ballast behaviour under dynamic loading. Part 1:A 2D polygonal discrete element method approach. *Computer Methods in Applied Mechanics and Engineering* 2006; **195**:2841–2859.
24. Alonso-Marroquin F. Spheropolygons: a new method to simulate conservative and dissipative interactions between 2D complex-shaped rigid bodies. *Europhysics Letters* 2008; **83**:14001.
25. Alonso-Marroquín F, Wang Y. An efficient algorithm for granular dynamics simulations with complex-shaped objects. *Granular Matter* 2009; **11**(5):317–329.
26. Galindo-Torres SA, Munoz JD. Minkowski–Voronoi diagrams as a method to generate random packings of spheropolygons for the simulation of soils. *Physical Review E* 2010; **82**: 056713.
27. Galindo-Torres SA, Pedroso DM, Williams DJ, Muhlhaus HB. Strength of non-spherical particles with anisotropic geometries under triaxial and shearing loading configurations. *Granular Matter* 2013; **15**:531–542.
28. Hopkins MA. Discrete element modeling with dilated particles. *Engineering Computations* 2003; **21**(2/3/4):422–430.
29. Hopkins MA. Polyhedra faster than spheres? *Engineering Computations* 2014; **31**(3):567–583.
30. Aursudkij B, McDowell GR, Collop AC. Cyclic loading of railway ballast under triaxial conditions and in a railway test facility. *Granular Matter* 2009; **11**:391–401.
31. Liu H, Zou D, Liu J. Constitutive modeling of dense gravelly soils subjected to cyclic loading. *International Journal for Numerical and Analytical Methods in Geomechanics* 2014; **38**:1503–1518.
32. Indraratna B, Thakur PK, Vinod JS, Salim W. A semi-empirical cyclic densification model for ballast incorporating particle breakage. *International Journal of Geomechanics* 2012; **12**(3):260–271.
33. Lu M, McDowell GR. Discrete element modelling of railway ballast under monotonic and cyclic triaxial loading. *Geotechnique* 2010; **60**(6):459–467.
34. Lackenby J, Indraratna B, Mcdowell G, Christie D. Effect of confining pressure on ballast degradation and deformation under cyclic triaxial loading. *Geotechnique* 2007; **57**(6):527–536.
35. Stahl M, Konietzky H. Discrete element simulation of ballast and gravel under special consideration of grain-shape, grain-size and relative density. *Granular Matter* 2011; **13**:417–428.
36. Wang YA. New algorithm to model the dynamics of 3-D bonded rigid bodies with rotations. *Acta Geotechnica* 2009; **4**:117–127.
37. Johnson KL. *Contact Mechanics*. Cambridge University Press: Cambridge, England, 1987.
38. Lin X, Ng T-T. A three-dimensional discrete element model using arrays of ellipsoids. *Geotechnique* 1997; **47** (2):319–329.
39. Ji SY, Shen HH. Internal parameters and regime map for soft polydispersed granular materials. *Journal of Rheology* 2008; **52**(1):87–103.
40. Indraratna B, Nimbalkar S. Stress–strain degradation response of railway ballast stabilized with geosynthetics. *Journal of Geotechnical and Geoenvironmental Engineering* 2013; **139**:684–700.

DOI: 10.1002/nag